

DOI: 10.1002/ ((please add manuscript number))

Article type: Full Paper

Shape-dependent Interactions of Palladium Nanocrystals with Hydrogen

*Anna Klinkova, Pavel V. Cherepanov, Ilya G. Ryabinkin, Martin Ho, Muthupandian Ashokkumar, Artur F. Izmaylov, Daria V. Andreeva, Eugenia Kumacheva**

Dr. A. Klinkova, Prof. Dr. E. Kumacheva

Department of Chemistry, University of Toronto, Toronto, Ontario M5S 3H6, Canada
E-mail: aklinkov@chem.utoronto.ca, ekumache@chem.utoronto.ca

Dr. P. Cherepanov, Dr. D. Andreeva

Physical Chemistry II, University of Bayreuth, Bayreuth 95440, Germany

Dr. I. G. Ryabinkin, M. Ho, Prof. Dr. A. F. Izmaylov

Physical and Environmental Sciences, University of Toronto Scarborough, Toronto, Ontario M1C 1A4, Canada

Prof. Dr. M. Ashokkumar

The School of Chemistry, University of Melbourne, Melbourne, Victoria 3010, Australia

Keywords: palladium nanoparticles, shape control, hydrogen, thermal stability, temperature programmed spectroscopy

Elucidation of the nature of hydrogen interactions with palladium nanoparticles is expected to play an important role in the development of new catalysts and hydrogen storage nanomaterials. A facile

This is the author manuscript accepted for publication and has undergone full peer review but has not been through the copyediting, typesetting, pagination and proofreading process, which may lead to differences between this version and the [Version of Record](#). Please cite this article as [doi: 10.1002/sml.201600015](https://doi.org/10.1002/sml.201600015).

This article is protected by copyright. All rights reserved.

scaled-up synthesis of uniformly sized single-crystalline palladium nanoparticles with various shapes, including regular nanocubes, nanocubes with protruded edges, rhombic dodecahedra, and branched nanoparticles, all stabilized with a mesoporous silica shell was developed. Interaction of hydrogen with these nanoparticles was studied by using temperature programmed desorption technique and by performing density functional theory modeling. It was found that due to favorable arrangement of Pd atoms on their surface, rhombic dodecahedral palladium nanoparticles enclosed by {110} planes release a larger volume of hydrogen and have a lower desorption energy than palladium nanocubes and branched nanoparticles. These results underline the important role of {110} surfaces in palladium nanoparticles in their interaction with hydrogen. This work provides insight into the mechanism of catalysis of hydrogenation/dehydrogenation reactions by palladium nanoparticles with different shapes.

1. Introduction

Over the past decade, metal nanoparticles (NPs) have attracted great attention as a new type of catalytic and hydrogen-storage materials.^[1-3] In particular, Pd NPs strongly absorb hydrogen and can be potentially used in hydrogen storage and purification.^[4-6] Moreover, Pd exhibits excellent catalytic properties in hydrogenation and dehydrogenation reactions.^[7] Recently, it has been established that hydrogen absorbed in the Pd subsurface region (the layer beneath the metal surface) plays a crucial role in these reactions.^[8-9] A high catalytic activity of Pd NPs in hydrogenation of alkenes was explained by the accessibility of hydrogen absorbed in this region, which was enhanced by the large NP surface area, in comparison with macroscopic Pd, in which hydrogen diffusing into the bulk metal is hardly accessible.^[8] Further studies of hydrogen adsorption and desorption on Pd NPs are important for the development of effective nanocatalysts for hydrogenation reactions^[10] and materials for hydrogen storage and purification.^[4]

In particular, it is expected that NP shape has a strong effect on their catalytic activity and hydrogen storage properties.^[7,11-19] Diffusion of hydrogen into and from the subsurface of metal NPs is influenced by the crystallographic facets enclosing a NP, thereby controlling its catalytic performance.^[20] The variation in the characteristic arrangement of atoms on the NP surface and the difference in surface energies of corresponding crystallographic facets explain different shape-

dependent performance of the NPs of the same metal in catalytic reactions.^[12,21] For example, in acetylene hydrogenation, a higher conversion efficiency of acetylene into ethylene on the surface of cubic Pd NPs was ascribed to the activation of Pd hydride and a weaker adsorption of organic species to {100} facets than in the case of spherical Pd NPs enclosed with mixed low index facets.^[22] In addition, the use of Pd NPs led to in approximately six-fold higher reaction rate than spherical NPs.^[22] It was also shown that the octahedral Pd NPs enclosed by {111} facets exhibit a higher hydrogen uptake rate than cubic NPs, enclosed by {100} planes.^[14] Hydrogen interactions with Pd NPs enclosed solely by {110} facets, to the best of our knowledge, have not yet been studied.

Another important consideration in the shape-controlled hydrogen absorption and catalytic performance of Pd NPs is the relative contribution of NP planes, edges and vertices. For example, different catalytic activity and selectivity of cubic, octahedral, and cuboctahedral Pd NPs in alkynol hydrogenation was attributed to a different fraction of NP planes and edges, which acted as active catalytic sites with different coordination numbers.^[17] Furthermore, edges and corners of Pd NPs play a crucial role in diffusion of hydrogen to the subsurface region in the process that is favored on low-coordination surface sites, that is, on NP edges.^[13] Development of understanding of the catalytic performance of Pd NPs with a different fraction of edges and planes, different angles between the planes and with enhanced accessibility of particular crystallographic planes for hydrogen would enable efficient rational design of catalysts and hydrogen storage materials

One of the challenges delaying such studies is the hurdle of producing uniformly sized and precisely shaped NPs in quantities that are sufficiently large, e.g., tens of milligrams of the sample for a single experiment, for the examination of hydrogen absorption/desorption isotherms, temperature programmed desorption, or temperature programmed reduction experiments. In addition, these experiments require the removal of organic capping agents used in NP synthesis, which may lead to

the change in NP shape and the loss in NP colloidal stability. Current synthetic protocols utilizing cationic surfactants are generally limited to <1 mg of Pd NPs.^[23-26] Synthetic methods that produce sub-gram amounts of Pd NPs,^[7] utilize polymer ligands (typically, polyvinylpyrrolidone) and yield Pd NPs with a limited shape range. A complete removal of ligands from NP surface is problematic. Presumably, studies of absorption and desorption of hydrogen with recently synthesized rhombic dodecahedral Pd NPs enclosed solely by {110} planes^[25] or cubic NPs with edge protrusions^[23] have been postponed due to the small-scale NP synthesis and the presence of a large excess of surfactant. Here we report a facile large scale synthesis of uniformly sized single-crystalline Pd NPs with various shapes, namely, nanocubes (NCs), rhombic dodecahedra (RDs), nanocubes with protruded edges (PNCs), and branched nanoparticles (BNPs). The NPs were stabilized with a thin mesoporous silica shell providing hydrogen access to the NP surface, while organic surfactant molecules were removed from the NP surface. For these NPs, we used the temperature-programmed desorption technique to explore the role of NPs morphology on their interactions with hydrogen. To gain insight into the mechanism of hydrogen adsorption on different sites of Pd NPs, we performed density functional theory (DFT) calculations. We show that Pd NPs enclosed by {110} planes exhibit a stronger release of hydrogen per unit surface area and a lower heat of adsorption, in comparison with NPs enclosed by {100} planes or mixed high index planes, which is preferred for catalytic reactions involving hydrogen and for efficient hydrogen storage. These findings provide important insight into the effect of Pd NP shape on their interactions with hydrogen. The results of our work can be used for the rational design of catalysts for hydrogenation/dehydrogenation reactions and hydrogen storage materials, as they underline a great importance of the {110} surfaces in NPs for the interaction with hydrogen.

2. Results and Discussion

This article is protected by copyright. All rights reserved.

2.1. Preparation of nanocrystals

2.1.1. Large-scale synthesis of Pd NPs

We synthesized Pd NPs with different shapes by scaling up seed-mediated synthetic methods reported for 5 mL scale reaction volume containing ~0.1 mg of Pd NPs.^[23-25] The scaled-up synthesis developed in the present work for Pd NCs, RDs, PNCs, and BNPs led to the yield of up to 70 mg of NPs for reaction volumes of 1 L, which was ~500-fold greater than in the methods reported for the synthesis of Pd NPs with such shapes^[23-25] The detailed synthetic protocols are described in Supporting Information.

Single crystalline Pd NCs were prepared by overgrowing single crystalline cubic Pd seeds at 45°C in the growth solution containing H_2PdCl_4 , ascorbic acid and cetyltrimethylammonium bromide (CTAB).^[23] The formation of cubic NPs was due to the presence of Br^- ions from the CTAB that are believed to adsorb to the surface of Pd NPs and promote the formation of the {100} facets.^[23] The resultant NCs had a 72 ± 3 nm side length (**Figure 1a** and Figure S1).

Palladium RDs were synthesized by the overgrowth on single-crystalline cubic Pd seeds at 80 °C in the growth solution in the presence of NaI. The introduction of NaI into the growth solution promoted the growth along the <100> direction of the Pd cubic seeds and the development of {110} and/or {111} facets during the NPs growth,^[25] due to the improved stability of these facets in the presence of I⁻ ions. The fraction of {110} and {111} facets in the NPs depended on reaction temperature.^[25] The scaled-up synthesis led to RDs with twelve well-defined {110} facets, similar to

the original small-scale procedure.^[25] The side length of the RDs was 45 ± 3 nm (Figure 1b, and Figure S2). We note that Pd octahedral NPs enclosed solely by $\{111\}$ planes could not be obtained using this method, as $\{111\}$ planes were not thermodynamically stable under the synthetic conditions and are only present in the NPs with mixed low index planes (for details see Supporting Information, section S2).

For scaled-up synthesis of PNCs, we introduced Cu(II) ions into the growth solution. During the reaction, Cu(II) selectively activated the fast growth of Pd along the $\langle 110 \rangle$ and $\langle 111 \rangle$ directions and promoted the formation of edge protrusions.^[23] A scaled-up procedure yielded PNCs with ~ 15 nm-high edge protrusions (Figures 1c and Figure S5). The side length of the PNC was 70 ± 4 nm, while the side of the inner cube was 40 ± 3 nm, as shown in inset in Figure 1c. The change of the shape of NPs in the scaled-up procedures occurred, possibly, due to the local concentration gradients and inhomogeneous reaction conditions.

The synthesis of the BNPs (Figure 1d and Figure S6) was conducted at $30\text{ }^{\circ}\text{C}$ by using the growth of Pd on the surface of small (~ 3 nm) Pd seeds in the growth solution containing Na_2PdCl_4 , Cu_2SO_4 , ascorbic acid, and CTAB.^[26] The presence of Cu(II) ions was responsible for the formation of branched structure by promoting the fast growth along $\langle 110 \rangle$ and $\langle 111 \rangle$ directions.

2.1.2. Encapsulation of Pd NPs with mesoporous silica

Ligands capping colloidal NPs can either decrease their catalytic activity by blocking the surface, or enhance their catalytic activity and/or selectivity *via* electronic effects, due to the charge transfer between the ligands and the NPs.^[27] In gas-phase heterogeneous catalytic reactions, ligands exert an

overall negative effect on the activity of catalytic NPs.^[27] Therefore in the present work, gas-phase studies of shape-dependent interactions of Pd NPs with hydrogen necessitated the removal of CTAB from the surface of as-synthesized Pd NPs. Since such a removal led to aggregation of ligand-deprived Pd NPs and a drastic reduction in their active surface area, the NPs were encapsulated with an inert thin mesoporous silica coating containing pores with a diameter of 3.5 ± 0.5 nm.^[28] The silica coating replaced CTAB and provided a spacer for the NPs studied in a gas atmosphere.

The CTAB molecules originally attached to the surface of Pd NPs were used as a template for three-dimensional polymerization of tetraethyl orthosilicate (TEOS), an alkoxide-based silica precursor, to form a mesoporous silica coating on the NPs. To remove excess CTAB prior to silica growth, no centrifugation was required, as the NPs settled on the bottom of the reaction flask in 12 h and the supernatant was removed by decantation (*see* Supporting Information for details).

The representative scanning electron microscopy (SEM) images of the silica-encapsulated NCs, RDs, PNCs, and BNPs (later in the text referred as NCs@SiO₂, RDs@SiO₂, PNCs@SiO₂, and BNPs@SiO₂, respectively) are shown in Figure 2a-d, S7-S9. Based on image analysis, the SiO₂ shell thickness was 12 ± 1 nm for NCs@SiO₂, 10 ± 1 for RDs@SiO₂, 11 ± 1 nm for PNCs@SiO₂ and 6 ± 2 nm for BNPs@SiO₂. The shape and the size uniformity of the Pd NPs did not change after the silica growth.

Mesoporous silica-modified NPs were separated from CTAB and free silica by five cycles of centrifugation, followed by NP redispersion in methanol. The removal of the positively charged CTAB surfactant from the surface of mesoporous silica-coated NPs was confirmed by measuring their electrokinetic potential, which gradually changed from ~ 50 mV to approximately -40 mV after 5 washing cycles (Figure S15).

2.1.3. Solid catalyst preparation and characterization

After surface modification and purification of the NPs, their methanol solutions were concentrated to a small (~1 mL) volume *via* centrifugation and the removal of the supernatant. The solution was drop-cast onto a glass slide, the solvent evaporated, and the resulting fine NP powder was isolated (Figure S12). A 1 L-scale synthesis typically produced up to 70 mg of mesoporous silica-coated NPs powder. The content of silica in all the NPs did not exceed 3 wt%, determined by inductively coupled plasma atomic emission spectroscopy (ICP-AES) analysis.

Prior to recording the TPD spectra, using XPS analysis we characterized the surface chemistry of all Pd nanocrystals. The results of XPS experiments indicated identical chemical compositions for all studied samples (Figure S16). The major peaks observed on the XPS spectra were: Si 2p (104.0 eV), Pd 3d (336.0 eV), and O 1s (533.0 eV). No Cu (933 eV), I (69 eV), or Br (619 eV) have been detected on the surface. In addition, this ensured that hydrogen interactions with Pd NPs are shape-dependent and are not governed by the differences in Pd oxidation state on the NP surface, as two peaks Pd 3d_{5/2} and 3d_{3/2} observed at 335.6 and 341 eV, respectively,^[29] were identical for all samples.

Thermal stability of the NPs was examined *in situ* imaging at high temperatures using environmental transmission electron microscopy (ETEM). Up to 400±10 °C, the NCs and RDs retained their shapes, with an insignificant truncation of the NP corners (Figure 3a, a', b, b'). These results agreed with the report on edge truncation of 20 nm-size Pd NCs at 400 °C.^[31] In contrast, strong truncation of protruded edges occurred for the PNCs at 400±10 °C (Figure 3c, c'), and significant rounding of NP branches in the BNP was observed at 350±10 °C (Figure 3d,

d'). Heat-induced shape transformations of the NPs were ascribed to a so-called pre-melting of the NP surface at the temperature lower than the melting point of the metal, due to the increased mobility of the atoms located at the NP surface.^[32]

2.2. Interaction of Pd nanocrystals with hydrogen

2.2.1. Temperature-programmed hydrogen desorption

The relationship between the shape of NPs and their interactions with hydrogen was explored using temperature-programmed desorption (TPD) technique. A 10% mixture of hydrogen with argon was purged through a Pd nanopowder for 15 min at a constant flow rate of 50 mL/min. To ensure that the amount of purged hydrogen was sufficient to occupy all available surface sites and to take into account possible diffusion hindrance of hydrogen towards the surface of Pd nanocrystals due to presence of ~10 nm-thick mesoporous silica a control experiment with higher excess of hydrogen (20% hydrogen/argon mixture) was performed. The recorded TPD spectra appeared to be identical (Figure S18), indicating no effect of silica shell porosity (pore size 3 nm) at the chosen pre-treatment conditions. Subsequent desorption of hydrogen from the differently shaped Pd NPs was monitored in the temperature range from 50 to 400°C at the heating rate of 10, 13, 15 and 18 °C/min. The selection of the temperature range was based on the physical properties of Pd NPs and the nature of hydrogen desorption. For example, above 400°C, the NPs changed their shape, as described above, while below 50°C, only physisorbed hydrogen was desorbing.^[32-33] In addition, to ensure that the porous silica shell does not interact with purged hydrogen, the control TPD profile was recorded for the control system,

namely, Pd-free mesoporous silica NPs prepared by the encapsulation of 67 ± 6 nm silica NPs with 10 nm-thick mesoporous silica shell (Figure S11). Hydrogen peaks were not observed in the resulting TPD spectrum (Figure S17), clearly indicating that the observed peaks corresponded to the hydrogen that desorbs from the Pd NPs surface and not from the silica shell.

Figure 4 shows the TPD profiles for hydrogen desorption from the surface of RDs@SiO₂, NCs@SiO₂, PNCs@SiO₂, and BNPs@SiO₂ recorded at the heating rate of 15 °C/min. For the first three NP types, strong desorption peaks were observed above 250 °C, while for BNPs@SiO₂ two distinct peaks existed at the lower temperatures. More specifically, the positions of the major peaks were 280 °C for RDs@SiO₂, 312 °C for NCs@SiO₂, and 288 °C for PNCs@SiO₂, and 250 °C and 187 °C for BNPs@SiO₂. In addition, for NCs@SiO₂ and PNCs@SiO₂, weaker secondary peaks were observed at 150 and 185 °C, respectively. For BNPs we also observed hydrogen desorption above 350 °C, presumably due to hydrogen desorption from the subsurface region probably caused by the BNP melting above this temperature.

The volume of hydrogen released per unit mass of the NPs was determined from the area under the peaks in the TPD spectra in Figure 4 and was related to the surface area of a particular NP type in assumption that the mesoporous silica layer blocks the same fraction of the surface of the NP with different shapes (*see* Section S12, Supporting Information). The PNCs@SiO₂ and NCs@SiO₂ released approximately equal volumes of hydrogen per surface area, while the RDs@SiO₂ released approximately two-fold larger volume of hydrogen per unit surface area. At the same time, BNPs@SiO₂ released a significantly lower volume of hydrogen per unit mass than other NP types, although their surface area was significantly larger than that of other NPs. The colors of the NP cartoons correspond to the colors of the TPD profiles.

Next, we determined the energy of hydrogen desorption on Pd NPs with different shapes by heating the NP powder at different rates. Figure 5a-d shows the dependence of hydrogen desorption temperature on the heating rate of the sample. The desorption activation energies of hydrogen were determined using the Kissinger (Redhead) equation $\ln\left(\frac{T_{max}^2}{\beta}\right) = \left(-\frac{E_a}{R}\right)\frac{1}{T_{max}} + K$, where β is the heating rate (K/min), T_{max} is the maximum peak temperature (K), E_a is the activation energy of desorption (kJ/mol), and R is the gas constant (8.314 J/mol K).^[34] The relationship of $\ln\left(\frac{T_{max}^2}{\beta}\right)$ and $\frac{1}{T_{max}}$ was plotted for the peaks observed in the TPD curves of different NP shapes (Fig. 5e-h) showing their linear dependence.

The slopes of the plots in Figure 5e-h corresponded to the desorption activation energies corresponding to the major peaks in the TPD spectra, which were found to be 82, 127, 117 kJ/mol for RDs@SiO₂, NCs@SiO₂, PNCs@SiO₂, respectively, and 62 and 72 kJ/mol for BNPs@SiO₂. For PNCs@SiO₂ for the secondary peak in the TPD spectra the desorption activation energy was 59 kJ/mol. In the case of the minor secondary peak for NCs@SiO₂, we observed inconsistency in the change of the peak maximum temperature with varying heating rate, which resulted in the non-linear dependence of $\ln\left(\frac{T_{max}^2}{\beta}\right)$ on $\frac{1}{T_{max}}$. This effect indicated changes in desorption kinetics, thereby violating the applicability of the Kissinger equation.

In addition to the NP shapes studied in this work, we performed TPD experiments on Pd nanoparticles with mixed low index surfaces including {111}, {110}, and {100} (Figure S3, S10). The corresponding TPD spectra were similar to the TPD spectra of RDs@SiO₂ and NCs@SiO₂ (Figure S19), while the hydrogen desorption activation energy was found to be 145 kJ/mol, that is, it was the highest of all the systems studied. This result suggested that the presence of {111} facets together with a higher fraction of edge atoms could be responsible for the overall increase in the

observed increase in desorption activation energy. Based on the results shown in Figure 4 and 5, we conclude that the NPs with a RD shape are preferred for reversible hydrogen adsorption, due to the lower heat of adsorption and greater amount of hydrogen released per unit surface area. On the other hand, while PNCs@SiO₂ possessed a nearly four-fold larger surface-to-mass ratio and thus release more hydrogen per unit mass, they showed a higher desorption energy and a lower hydrogen release per unit surface area than RDs@SiO₂ and NCs@SiO₂. A similar trend was observed for BNPs@SiO₂: in spite of the large surface area of these NPs, they released the lowest hydrogen volume, in comparison with other NP types. This effect can be attributed to the presence of high-index facets and surface defects, which allowed easier hydrogen penetration into the bulk. Therefore, for these NPs hydrogen release was governed by the surface/bulk interactions of hydrogen, rather than the NP surface area. To gain better understanding of the observed trends, we characterized hydrogen adsorption energies for different sites on Pd NPs using DFT simulations.

2.2.2. DFT Simulations

To obtain further insights into hydrogen desorption from NPs with different shapes, we carried out calculations of hydrogen adsorption energies for various NP sites as

$E_{\text{ads,A}}(\text{H}_2) = 2(E[\text{site A} + \text{H}] - E[\text{site A}] - E[\text{H}_2])$, where $E[\text{site A} + \text{H}]$ and $E[\text{site A}]$ are geometrically optimized electronic energies of an adsorption site A with and without the hydrogen atom, respectively, and $E[\text{H}_2]$ is the electronic energy of the hydrogen molecule in gas phase. Hydrogen-palladium adsorption energies were determined using DFT with the Perdew-Burke-Ernzerhof (PBE) exchange correlation functional and the Grimme D2 dispersion correction^[35,36] implemented in the

Quantum Espresso ab initio program^[37] (see Supporting Information for further computational details). The surfaces and ridges of the NPs have been modeled as infinite periodic slabs. Amorphous silica coating was not taken into account in the calculations assuming that it does not exhibit selectivity for specific adsorption sites and randomly covers a fraction of the NP surface.

Figure 6a-c shows the arrangement of surface atoms on idealized NCs, RDs, and PNCs (the SiO₂ shell is not shown).^[38] While the NCs and RDs are enclosed exclusively by {100} and {110} facets, respectively, PNCs are enclosed by at least, two different types of facets. More specifically, the cubic fragment of PNC has {100} facets, and the idealized protrusions along <110> directions are enclosed by {110} facets. We note that in the real PNCs, the transition between the cubic constituent and protrusions is somewhat smeared (see Figures 1c, S5), which leads to uncertainty in the surface arrangement of atoms. A similar argument applies to BNPs. For this reason, DFT simulations were limited to the (110) and (100) surfaces (see Figure 6d-e).

To relate calculated adsorption energies with measured activation desorption energies we assumed that the thermal desorption process includes the following two steps:



where the desorption step uses the formation energy of the hydrogen molecule ($D_0 = 432$ kJ/mol in the gas phase^[39]) released in the recombination step. The alternative mechanism, in which atomic hydrogen desorption is followed by hydrogen recombination in the gas phase, would have a large desorption activation energy exceeding 400 kJ/mol, because individual atoms adsorbed on the surface sites cannot use the recombination energy for their desorption. Since all experimental activation energies were lower than 130 kJ/mol, the mechanism involving direct atomic hydrogen desorption was ignored.

To compare adsorption energies determined in the calculations with desorption activation energies determined in the TPD experiments, the adsorption energies have been averaged to account for the surface diffusion of adsorbed hydrogen in the recombination step (Table 1). For both surfaces, the averaging procedure utilized equal weights for all site energies, due to the equal numbers of occurrences of different surface sites per unit cell. The desorption activation energies determined from the maxima of the TPD peaks (Figure 5) agreed with the calculated averaged adsorption energies for different surface sites on NPs with different shapes (Figure 6d-e). In particular, all stable sites on the (110) surface had an average adsorption energy of 89 kJ/mol, in agreement with experimentally determined energy of 82 kJ/mol for RDs@SiO₂. The calculated averaged adsorption energy of the (100) surface for the “bridge” and “hollow” positions (Figure 6d) was 107 kJ/mol, that is, reasonably close to the experimentally determined desorption energy of 127 kJ/mol for NCs@SiO₂. A more accurate site energy averaging procedure would require explicit consideration of the diffusion process and thus is beyond the scope of the current study.

DFT simulations for Pd {111} facets resulted in the calculated average adsorption energy value of 126 kJ / mol (Table 1), which is higher than those of {100} and {110}. Thus, we observed the trend, in which the adsorption energy is increasing in the row {110} < {100} < {111}. To verify that the same trend could be observed experimentally, we recorded the TPD spectra for the Pd nanocrystals enclosed by {111}, {100}, and {110} facets. According to DFT simulations, the presence of {111} planes should increase the value of adsorption energy compared with that of Pd nanocrystals enclosed by only {100} or {110} facets. Indeed, the experimentally determined value of adsorption energy for such particles was found to be 145 kJ / mol, which confirmed the theoretically established trend.

Hydrogen adsorption on NP ridges did not exhibit any peculiar features: adsorption energies of stable sites on ridges of NCs and RDs were only marginally different from the adsorption energies of the NP planes. Moreover, since there is a significantly smaller number of Pd atoms on the NP ridges than on the planes, the NP ridges were unlikely to contribute significantly to the thermodynamics and kinetics of the hydrogen desorption.

3. Conclusion

We developed large-scale synthesis of uniformly sized Pd NPs with various shapes and explored hydrogen adsorption and desorption on these NPs using temperature programmed desorption technique and DFT simulations. We showed that hydrogen release from the NPs depends on its surface/bulk interactions with NPs, rather than the NP surface area. We found that rhombic dodecahedral Pd NPs enclosed by $\{110\}$ planes show a higher volume of hydrogen desorbed per surface area and a lower desorption hydrogen energy, in comparison with regular Pd nanocubes, nanocubes with protruded edges and branched NPs, due to the difference in the exposed surface planes.

These findings provide insights into the nature of hydrogen interaction with differently shaped Pd NPs enclosed by different planes. In particular, our results underline the importance of $\{110\}$ surfaces in NPs for their interaction with hydrogen. Furthermore, we show that branched Pd NPs with ill-defined surfaces allow easier hydrogen penetration into the bulk, possibly due to the presence of surface defects and high index planes. These findings can play an important role in the development

of efficient hydrogen storage nanomaterials and shed light on the mechanism of catalysis of hydrogenation/ dehydrogenation reactions by NPs with controllable shapes.

Supporting Information

Supporting Information is available from the Wiley Online Library or from the author.

Acknowledgements

AK thanks I. Gourevich and N. Coombs for help with SEM imaging, and C. Soong for help with *in situ* heating TEM experiments. AK and EK thank Connaught fund for financial support of this work. AK acknowledges Ontario Trillium Scholarship. AFI greatly appreciates financial support by Alfred P. Sloan Foundation and NSERC of Canada through the Discovery Grants Program. PVC, AM, DVA thank the DAAD (German Academic Exchange Service) funded by the BMBF (Federal Ministry of Education and Research) within the program Strategic Partnerships and Thematic Networks and the Bayreuth-Melbourne Colloid/Polymer-Network (Project-ID 57173303) for financial support.

Received: ((will be filled in by the editorial staff))

Revised: ((will be filled in by the editorial staff))

Published online: ((will be filled in by the editorial staff))

- [1] M. Yamauchi, R. Ikeda, H. Kitagawa, M. J. Takata, *Phys. Chem. C* **2008**, *112*, 3294.
- [2] M. Yamauchi, H. Kobayashi, H. Kitagawa, *ChemPhysChem* **2009**, *10*, 2566.

This article is protected by copyright. All rights reserved.

- [3] H. Kobayashi, H. Morita, M. Yamauchi, R. Ikeda, H. Kitagawa, Y. Kubota, K. Kato, M. Takata, *J. Am. Chem. Soc.* **2012**, *134*, 12390.
- [4] D. P. Broom, *Hydrogen Storage Materials: The Characterization of Their Storage Properties*. Springer: London, **2011**.
- [5] A. W. C. van den Berg, C. O. Arean C. O. *Chem. Commun.*, **2008**, 668.
- [6] F. Raimondi, G. G. Scherer, R. Kotz, A. Wokaun *Angew. Chem. Int. Ed.* **2005**, *44*, 2190.
- [7] Xia, Y.; Xiong, Y.; Lim, B.; Skrabalak, S. E. Shape-Controlled Synthesis of Metal Nanocrystals: Simple Chemistry Meets Complex Physics? *Angew. Chem. Int. Ed.* **2009**, *48*, 60–103.
- [8] A. M. Doyle, S. K. Shaikhutdinov, S. D. Jackson, H.-J. Freund, *Angew. Chem. Int. Ed. Engl.* **2003**, *42*, 5240.
- [9] D. Teschner, J. Borsodi, A. Wootsch, Z. Révay, M. Hävecker, A. Knop-Gericke, S. D. Jackson, R. Schlögl, *Science* **2008**, *320*, 86.
- [10] D. Astruc *Nanoparticles and Catalysis*. Wiley-VCH: Weinheim, **2008**.
- [11] H. U. I. Zhang, M. Jin, Y. Xiong, B. Lim, Y. Xia, *Acc. Chem. Res.* **2013**, *46*, 1783.
- [12] A. Ruditskiy, S.-I. Choi, H.-C. Peng, Y. Xia, *MRS Bull.* **2014**, *39*, 727.
- [13] W. Ludwig, A. Savara, R. J. Madix, S. Schauer mann, H.-J. Freund, *J. Phys. Chem. C* **2012**, *116*, 3539.

- [14] G. Li, H. Kobayashi, S. Dekura, R. Ikeda, Y. Kubota, K. Kato, M. Takata, T. Yamamoto, S. Matsumura, H. Kitagawa, *J. Am. Chem. Soc.* **2014**, *136*, 10222.
- [15] A. R. Tao, S. Habas, P. Yang, *Small* **2008**, *4*, 310.
- [16] J. Gu, Y. W. Zhang, F. Tao, *Chem. Soc. Rev.* **2012**, *41*, 8050.
- [17] M. Crespo-Quesada, A. Yarulin, M. Jin, Y. Xia, Y.; L. Kiwi-Minsker, *J. Am. Chem. Soc.* **2011**, *133*, 12787.
- [18] M. Laskar, S. Skrabalak, *ACS Catal.* **2014**, *4*, 1120.
- [19] S. Wang, W. Zhu, J. Ke, M. Lin, Y. Zhang, *ACS Catal.*, **2014**, *4*, 2298.
- [20] W. Ludwig, A. Savara, S. Schauermaun, H.-J. Freund, *ChemPhysChem.* **2010**, *11*, 2319.
- [21] C. Burda, X. Chen, R. Narayanan, M. A. El-Sayed, *Chem. Rev.* **2005**, *105*, 1025.
- [22] S. K. Kim, C. Kim, J. H. Lee, J. Kim, H. Lee, S. H. Moon, *J. Catal.* **2013**, *306*, 146.
- [23] W. Niu, W. Zhang, S. Firdoz, X. Lu, *Chem. Mater.* **2014**, *26*, 2180.
- [24] W. Niu, Z.-Y. Li, L. Shi, X. Liu, H. Li, S. Han, J. Chen, G. Xu *Cryst. Growth Des.* **2008**, *8*, 4440–4444.
- [25] W. Niu, L. Zhang, G. Xu, **2010**, *4*, 1987.
- [26] Y. H. Chen, H. H. Hung, M. H. Huang, *J. Am. Chem. Soc.* **2009**, *131*, 9114.
- [27] W. Huang, Q. Hua, T. Cao, *Catal. Letters* **2014**, *144*, 1355.
- [28] I. Gorelikov, N. Matsuura, *Nano Lett.* **2008**, *8*, 369.

- [29] J. F. Moulder, W. F. Stickle, P. E. Sobol, K. D. Bomben, *Handbook of X-ray Photoelectron Spectroscopy*. Perkin Elmer: Waltham, MA, **1995**.
- [30] N. Lu, J. Wang, S. Xie, Y. Xia, M. J. Kim, *Chem. Commun.* **2013**, 49, 11806.
- [31] S. J. Mejia-Rosales, C. Fernandez-Navarro, E. Perez-Tijerina, J. M. Montejano-Carrizales and M. Jose-Yacamán, *J. Phys. Chem. B*, **2006**, 110, 12884–12889.
- [32] S. L. M. Schroeder, M. Gottfried, *Temperature-Programmed Desorption (TPD) Thermal Desorption Spectroscopy (TDS)*. Advanced Physical Chemistry Laboratory: FU Berlin, **2002**.
- [33] R. I. Masel, *Principles of Adsorption and Reaction on Solid Surfaces*, Wiley: New York, **1996**.
- [34] P. A. Redhead, *Vacuum* **1962**, 12, 203.
- [35] S. Grimme, *S. J. Comput. Chem.* **2006**, 27, 1787.
- [36] V. Barone, M. Casarin, D. Forrer, M. Pavone, M. Sambri, A. Vittadini, *J. Comput. Chem.* **2009**, 30, 934.
- [37] P. Giannozzi, S. Baroni, N. Bonini, M. Calandra, R. Car, C. Cavazzoni, D. Ceresoli, G. L. Chiarotti, M. Cococcioni, I. Dabo, A. Dal Corso, S. de Gironcoli, S. Fabris, G. Fratesi, R. Gebauer, U. Gerstmann, C. Gougoussis, A. Kokalj, M. Lazzeri, L. Martin-Samos, N. Marzari, F. Mauri, R. Mazzarello, S. Paolini, A. Pasquarello, L. Paulatto, C. Sbraccia, S. Scandolo, G. Sclauzero, A. P. Seitsonen, A. Smogunov, P. Umari, R. M. Wentzcovitch, *J. Phys.: Condens. Matter* **2009**, 21, 395502.

[38] M. De Graef, M. McHenry, *Structure of Materials: an Introduction to Crystallography, Diffraction, and Symmetry*, 2nd ed.; Cambridge University Press: New York, **2012**.

[39] G. Herzberg, *Phys. Rev. Lett.* **1969**, *23*, 1081.

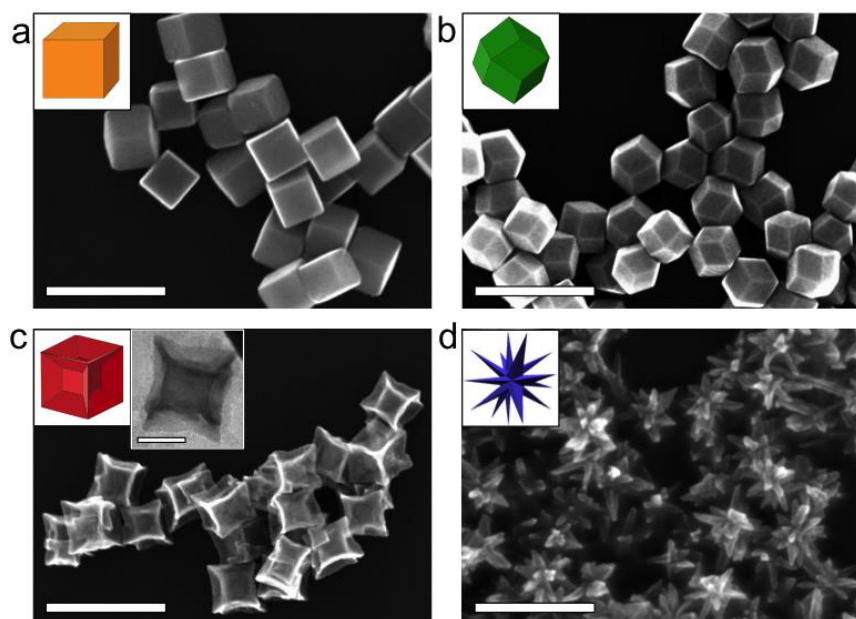


Figure 1. SEM images of Pd NCs (a), RDs (b), PNCs (c), and BNPs (d). Scale bars are 200 nm. The TEM image of a PNC is shown in the inset of Figure (c), scale bar is 50 nm. Insets in (a-d) show the cartoons of corresponding NPs.

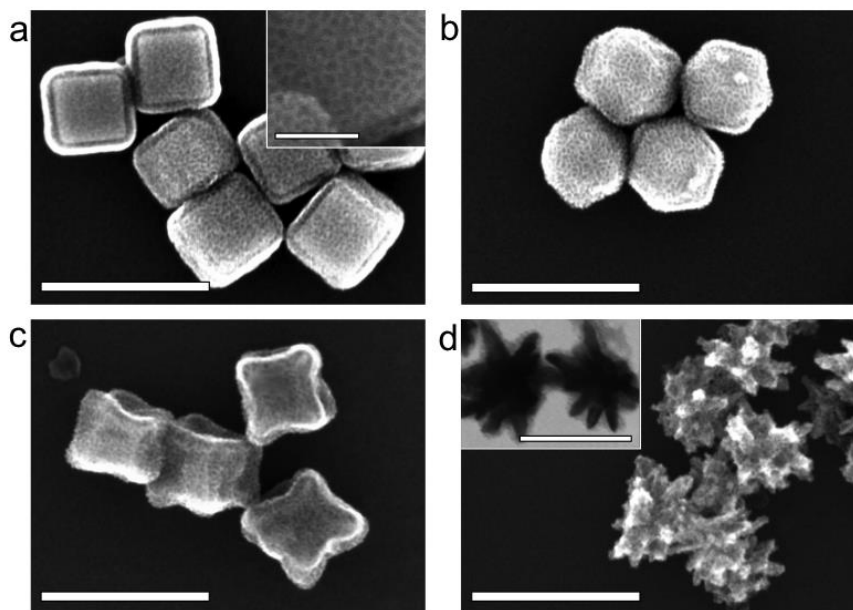
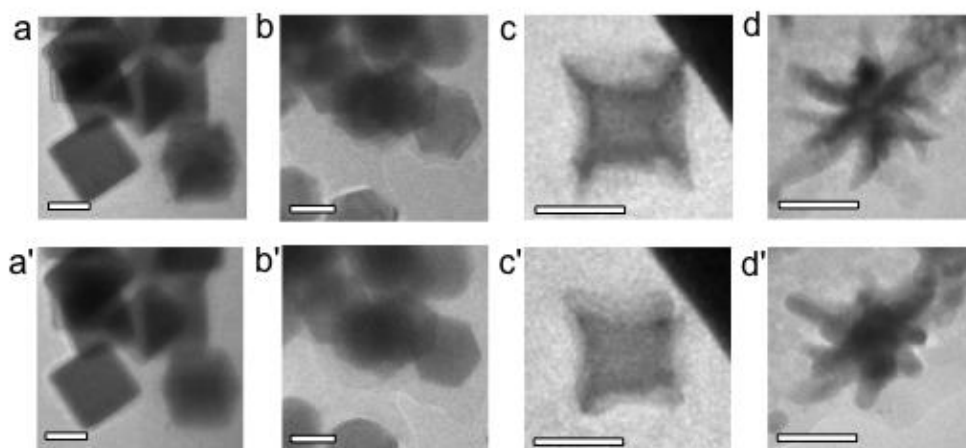


Figure 2. SEM images of NCs@SiO₂ (a), RDs@SiO₂ (b), PNCs@SiO₂ (c), and

BNPs@SiO₂ (d) Scale bars are 200 nm. The inset in (a) is a high-magnification SEM image

of NCs@SiO₂ Scale bar is 25 nm. The inset in (d) shows a TEM image of BNPs@SiO₂. Scale bar is 100 nm.



This article is protected by copyright. All rights reserved.

Figure 3. *In situ* TEM heating images of different NP shapes at ambient temperature (a, b, c, d) and after being heated to 400 °C. (a', b', c', d'): (a, a') NCs@SiO₂, (b, b') RDs@SiO₂, (c, c') PNCs@SiO₂, and (d, d') BNPs@SiO₂.

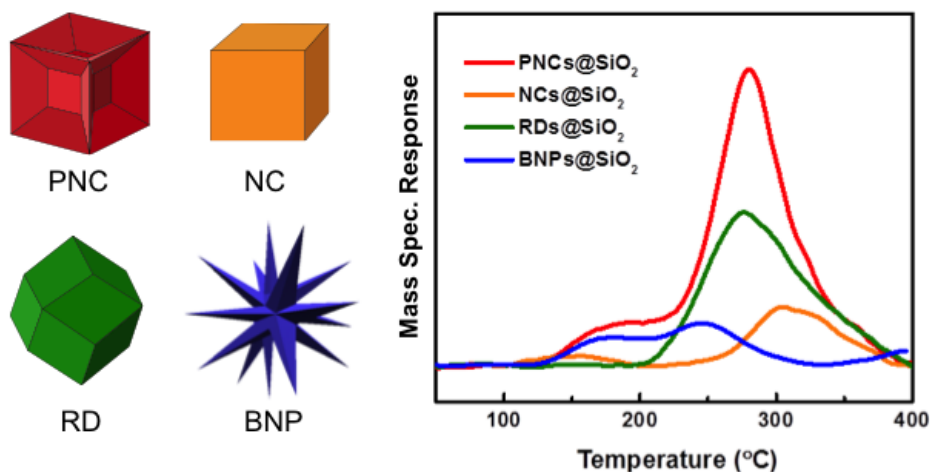


Figure 4. Illustration of Pd nanocrystals (left) and TPD spectra (right) of RDs@SiO₂ (green), NCs@SiO₂ (orange), PNCs@SiO₂ (red), and BNPs@SiO₂ (blue) at 15 °C /min heating rate. The spectra are normalized with respect to desorbed volume of hydrogen per unit mass. The colors of the NP cartoons correspond to the colors of the TPD profiles.

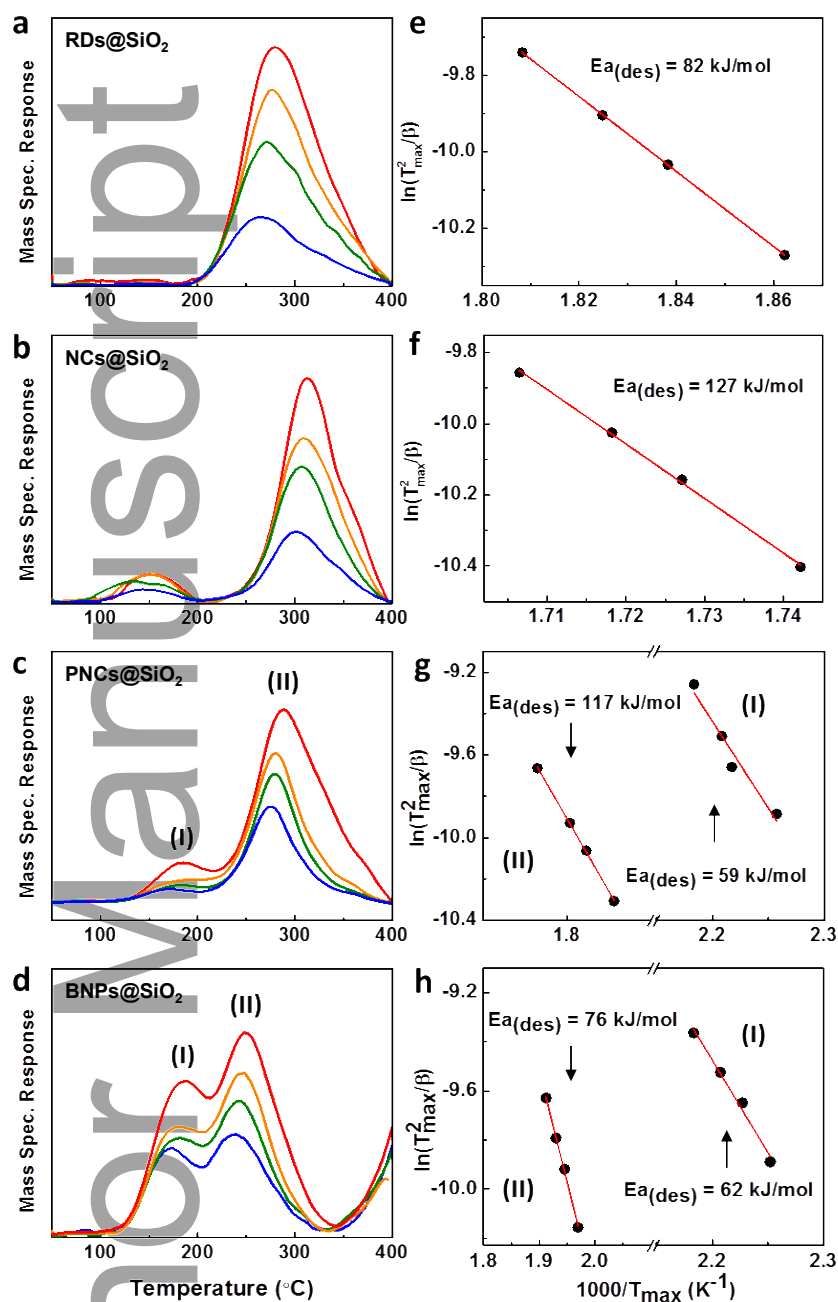


Figure 5. (a-d) TPD spectra of RDs@SiO₂ (a), NCs@SiO₂ (b), PNCs@SiO₂ (c), and BNPs@SiO₂ (d) recorded at heating rates of 18 °C/min (red), 15 °C/min (orange), 13 °C/min (green), and 10 °C/min (blue). (e-h) Determination of desorption energy from the variation of $\ln(T_{\max}^2/\beta)$ vs. $1000/T_{\max}$ (K⁻¹), plotted for major peaks at RDs@SiO₂ (e), NCs@SiO₂ (f), PNCs@SiO₂ (g), and BNPs@SiO₂ (h).

This article is protected by copyright. All rights reserved.

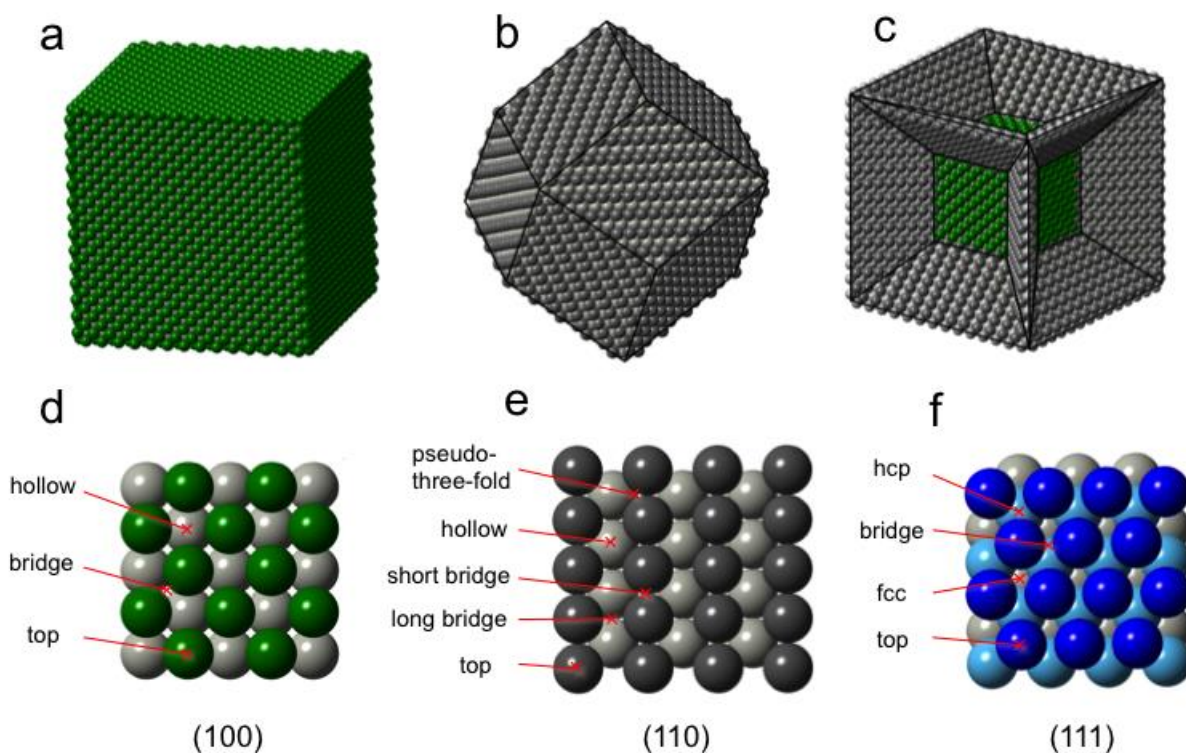


Figure 6. (a-c) Model crystalline structure of metal NPs with different idealized shapes with *fcc* lattice. (a) Cube enclosed by {100} facets. (b) Rhombic dodecahedron enclosed by {110} facets. (c) Cube with edge protrusions: the inner cube is enclosed by {100} facets, and protrusions have exposed {110} facets. (d-f) Schematic representation of adsorption sites on low-index facet surfaces of Pd: (d) Pd (100) plane, (e) Pd (110) plane, and (f) Pd (111) plane.

System	Adsorption site	$E_{ad}(H_2)$, kJ/mol	Average calculated $E_{ad}(H_2)$	Measured $E_{ad}(H_2)$, kJ/mol
on a surface				
(100) - NC	Top	unstable		
	Bridge	110	108	127
	Hollow	105		
(110) - RD	Top	unstable		
	Long bridge	97.3		
	Short bridge	86.4	89.0	82.0
	Hollow	58.5		
	Pseudo-three-fold	114		
(111)	Top	28.9		
	Bridge	unstable		
	Hexagonal-close-packed	121	126	
	Face-centered-cubic	130		
on a ridge				
[(100)/(100)] - NC	Top	unstable		
	Bridge	113		
[110/110] - RD	Top	unstable		
	Bridge	103		

Table 1. Adsorption energies of hydrogen for selected surfaces and ridges.

Author Manuscript

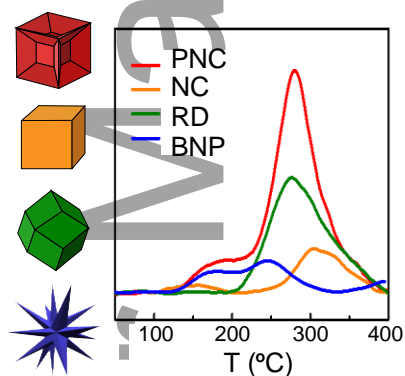
This article is protected by copyright. All rights reserved.

Hydrogen-palladium interactions were studied on a series of Pd nanoparticles with various well-defined shapes. We developed a facile scaled-up synthesis of monodisperse palladium nanoparticles with various shapes, stabilized with a mesoporous silica shell. Hydrogen-nanoparticle interactions were studied using temperature programmed desorption and DFT modeling. These findings help to elucidate the nature of hydrogen interactions with palladium nanoparticles of different shapes.

palladium nanoparticles, shape control, hydrogen, thermal stability, temperature programmed spectroscopy

A. Klinkova, P. V. Cherepanov, I. G. Ryabinkin, M. Ho, M. Ashokkumar, A. F. Izmaylov, D. V. Andreeva, E. Kumacheva*

Shape-dependent Interactions of Palladium Nanocrystals with Hydrogen



This article is protected by copyright. All rights reserved.